10. E.I. Thorsos, The calidity of the Kirchhoff approximation for rough surface scattering using a Gaussian roughness spectrum, J Acoust Soc Am 83 (1988), 78–84.
11. L. Tsang, J.A. Kong, K.H. Ding, and C.O. Ao, Scattering of electromagnetic waves—Numerical simulations, Wiley, Hoboken, NJ, 2001.

APPLICATION OF THE HIGH-ORDER SYMPLECTIC FDTD SCHEME TO THE CURVED THREE-DIMENSIONAL PERFECTLY CONDUCTING OBJECTS

Wei Sha, Xianliang Wu, Mingsheng Chen, and Zhixiang Huang
Key Laboratory of Intelligent Computing & Signal Processing, Anhui University, Hefei 230039, China

Received 3 September 2006

ABSTRACT: *A high-order symplectic finite-difference time-domain (SFDTD) scheme using the diagonal split-cell model is presented to analyze electromagnetic scattering of the curved three-dimensional perfectly conducting objects. On the one hand, for the undistorted cells, the fourth-order accurate spatial difference is employed. On the other hand, for the completely distorted cells, the treatment of the curved surfaces is based on the diagonal split-cell model. Finally, for the partially distorted cells, the interpolation strategy is proposed to keep the field components continuous. The numerical experiments suggest that the diagonal SFDTD scheme can obtain more accurate results than both the staircased SFDTD scheme and the traditional diagonal FDTD method. Furthermore, in view of the high numerical stability, the improved symplectic scheme does not need to decrease time increment to comply with the stability criterion.* © 2007 Wiley Periodicals, Inc. Microwave Opt Technol Lett 49: 931–934, 2007; Published online in Wiley InterScience (www.interscience.wiley.com). DOI 10.1002/mop.22306

Key words: *symplectic integrator; curved conducting surfaces; diagonal split-cell model; high-order difference; radar cross section*

1. INTRODUCTION

As the most standard algorithm, the traditional finite-difference time-domain (FDTD) method [1], which is second-order accurate in both space and time, has been widely applied to the electromagnetic computation and simulation. Unfortunately, for electrically large domains and for long-term simulation, the method consumes large computational resources owing to the limit of numerical dispersion and stability. Up to now, some more efficient solutions have been presented. For example, in 1989, Fang proposed high-order accurate FDTD method [2], which is fourth-order accurate in both space and time. But the method is hard to treat the varying of permittivity and permeability in the inhomogeneous domain on account of the application of third-order spatial derivatives to substitute for third-order correctional temporal derivatives. Another approach is to use fourth-order accurate Runge–Kutta method [3] in the time direction and central-difference with Yee lattice in the space direction; yet, the method is dissipative and requires additional memory.

The symplectic schemes have demonstrated their advantage in energy conservation for the Hamiltonian system over other high-order methods [4]. A symplectic FDTD (SFDTD) scheme [5, 6], which is explicit fourth-order accurate in both space and time, was introduced to the computational electromagnetism by Hirono for analyzing waveguide's eigenmode. It has been verified that the SFDTD scheme is nondissipative and saves memory. Moreover, the total field and scattered field technique and the near-to-far-field transformation [7, 8] have been further developed, by which the radar cross section (RCS) of dielectric sphere was successfully computed.

However, considering the high-order difference approximation for the spatial derivatives and the staircase model for the curved surfaces, the advantage of the SFDTD scheme cannot extend to electromagnetic scattering of the curved three-dimensional perfectly conducting objects. Here, the diagonal SFDTD scheme is presented to overcome the problem. The Yee cells in the scheme are classified and discriminatingly handled, which not only eliminates the spurious solutions, but also maintains the numerical results accurate.

The paper is organized as follows. The formulation of the SFDTD scheme is given in section 2, followed by the diagonal split-cell model for treating curved surfaces specified in section 3, numerical results are presented in section 4, and summary is concluded in section 5.

2. GENERAL FORMULATION

The following notation for a function of space and time on a Cartesian grid is introduced as

$$F(x,y,z,t) = F(i\Delta_x, j\Delta_y, k\Delta_z, (n + l/m)\Delta_t) \tag{1}$$

where Δ_x, Δ_y, Δ_z are, respectively, the lattice space increments in the x, y, and z coordinate directions, Δ_t is the time increment, i, j, k, n, l, and m are integers, $n + l/m$ denotes the $l - th$ stage after the $n - th$ time step, and m is the total stage number.

As for the space direction, centered finite-difference expressions are used to discretize the first-order spatial derivatives, as follows

$$\left(\frac{\partial F^{n+l/m}}{\partial \delta}\right)_h \approx \lambda_1 \frac{F^{n+l/m}(h + 1/2) - F^{n+l/m}(h - 1/2)}{\Delta_\delta} + \lambda_2 \frac{F^{n+l/m}(h + 3/2) - F^{n+l/m}(h - 3/2)}{3\Delta_\delta} \tag{2}$$

where $\delta = x,y,z$, $h = i,j,k$, and $\lambda_1 + \lambda_2 = 1$. In addition, when $\lambda_1 = 1$, the expressions are second-order accurate in space, and when $\lambda_1 = 9/8$, those are fourth-order accurate in space.

Maxwell's equations in the free space can be written in matrix form as [6]

$$\frac{\partial}{\partial t}\begin{pmatrix}\mathbf{H}\\ \mathbf{E}\end{pmatrix} = (A + B)\begin{pmatrix}\mathbf{H}\\ \mathbf{E}\end{pmatrix} \tag{3}$$

$$A = \begin{pmatrix}\{0\}_{3\times3} & \{0\}_{3\times3}\\ \varepsilon_0^{-1}R & \{0\}_{3\times3}\end{pmatrix} \quad B = \begin{pmatrix}\{0\}_{3\times3} & -\mu_0^{-1}R\\ \{0\}_{3\times3} & \{0\}_{3\times3}\end{pmatrix} \tag{4}$$

$$R = \begin{pmatrix} 0 & -\frac{\partial}{\partial z} & \frac{\partial}{\partial y}\\ \frac{\partial}{\partial z} & 0 & -\frac{\partial}{\partial x}\\ -\frac{\partial}{\partial y} & \frac{\partial}{\partial x} & 0 \end{pmatrix} \tag{5}$$

where $\mathbf{E} = (E_x, E_y, E_z)^{\mathrm{T}}$ is the electric field vector and $\mathbf{H} = (H_x, H_y, H_z)^{\mathrm{T}}$ is the magnetic filed vector, $\varepsilon_0$and μ_0 are the permittivity and permeability of the free space, $\{0\}_{3\times3}$ is the 3×3 null matrix, and R is the 3×3 matrix representing the three-dimensional curl operator.

Using the product of elementary symplectic mapping, the exact solution of Eq. (3) during the time step Δ_t can be approximately constructed as [9]

$$\exp(\Delta_t(A+B)) = \prod_{l=1}^{m} \mathrm{xp}(c_l\Delta_t B)\exp(d_l\Delta_t A) + O((\Delta_t)^{p+1}) \quad (6)$$

where c_l and d_l are the constant coefficients of the symplectic integrator, p is the order of the approximation. Here we use $m = 5$ and $p = 4$, a five-stage fourth-order symplectic integrator is obtained. The coefficients can be found in [6].

The formulation of the x component of the normalized electric field ($\tilde{E}_x = \sqrt{\varepsilon_0/\mu_0}E_x$) for the SFDTD scheme can be written as

$$\begin{aligned}
\tilde{E}_x^{n+l/m}\left(i+\frac{1}{2},j,k\right) &= \tilde{E}_x^{n+(l-1)/m}\left(i+\frac{1}{2},j,k\right) + d_l \times \Bigg\{ \lambda_l \times \Bigg[\mathrm{CFL}_y \\
&\times \left(H_z^{n+(l-1)/m}\left(i+\frac{1}{2},j+\frac{1}{2},k\right) - H_z^{n+(l-1)/m}\left(i+\frac{1}{2},j-\frac{1}{2},k\right)\right) \\
&- \mathrm{CFL}_z \times \left(H_y^{n+(l-1)/m}\left(i+\frac{1}{2},j,k+\frac{1}{2}\right) - H_y^{n+(l-1)/m}\left(i+\frac{1}{2},j,k\right.\right. \\
&\left.\left. -\frac{1}{2}\right)\right)\Bigg] + \left(\frac{\lambda_2}{3}\right) \times \Bigg[\mathrm{CFL}_y \times \left(H_z^{n+(l-1)/m}\left(i+\frac{1}{2},j+\frac{3}{2},k\right)\right. \\
&\left. - H_z^{n+(l-1)/m}\left(i+\frac{1}{2},j-\frac{3}{2},k\right)\right) - \mathrm{CFL}_z \times \left(H_y^{n+(l-1)/m}\left(i+\frac{1}{2},j,k\right.\right. \\
&\left.\left. +\frac{3}{2}\right) - H_y^{n+(l-1)/m}\left(i+\frac{1}{2},j,k-\frac{3}{2}\right)\right)\Bigg]\Bigg\} \quad (7)
\end{aligned}$$

$$\mathrm{CFL}_y = \frac{1}{\sqrt{\mu_0\varepsilon_0}}\frac{\Delta_t}{\Delta_y}, \mathrm{CFL}_z = \frac{1}{\sqrt{\mu_0\varepsilon_0}}\frac{\Delta_t}{\Delta_z} \quad (8)$$

For the cubic lattice case, $\Delta_x = \Delta_y = \Delta_z = \Delta_\delta$, then $\mathrm{CFL}_x = \mathrm{CFL}_y = \mathrm{CFL}_z = \mathrm{CFL}_\delta$. The uniform constant CFL_δ is called Courant–Friedrichs–Levy (CFL) number.

3. DIAGONAL SPLIT-CELL MODEL

For high-order spatial difference, every H-component is surrounded by eight E-components, and vice versa. In Figure 1(a), the near four circulating E-components equidistant to the H-component can link one closed loop referred to as L_1, and those far can link another loop L_2. The closed PEC surface is notated by S. The L_1, L_2, and S can be viewed as the point set. We treat all the cells drawn in Figures 1(b)–1(d) according to the following strategies.

1. *Undistorted cells* ($(L_1 \cup L_2) \cap S = \emptyset$). Here the fourth-order spatial difference is employed. The parameter λ_1 and λ_2 in Eq. (7) are taken to be 9/8 and $-$ 1/8.
2. *Completely distorted cells* ($L_1 \cap S \neq \emptyset$). The E-fields are treated in the traditional staircased FDTD way by setting $\lambda_1 = 1$ and $\lambda_2 = 0$. The H-fields are handled according to the diagonal split-cell model [10]. If and only if the near circulating E-fields are designated as split along the cell diagonal, the H-fields are to be updated by setting $\lambda_1 = 2$ and $\lambda_2 = 0$. Besides, $\lambda_1 = 1$ and $\lambda_2 = 0$ should be set.
3. *Partially distorted cells* ($(L_1 \cap S) = \emptyset$ *and* $L_2 \cap S) \neq \emptyset$). Both E-fields and H-fields are initially computed by using the traditional staircased FDTD approach. Then, to eliminate the reflection from the undistorted cells to the completely distorted cells, the partially distorted cells are specially treated to keep the field components continuous. The interpolation equations for the E-fields and H-fields are proposed as

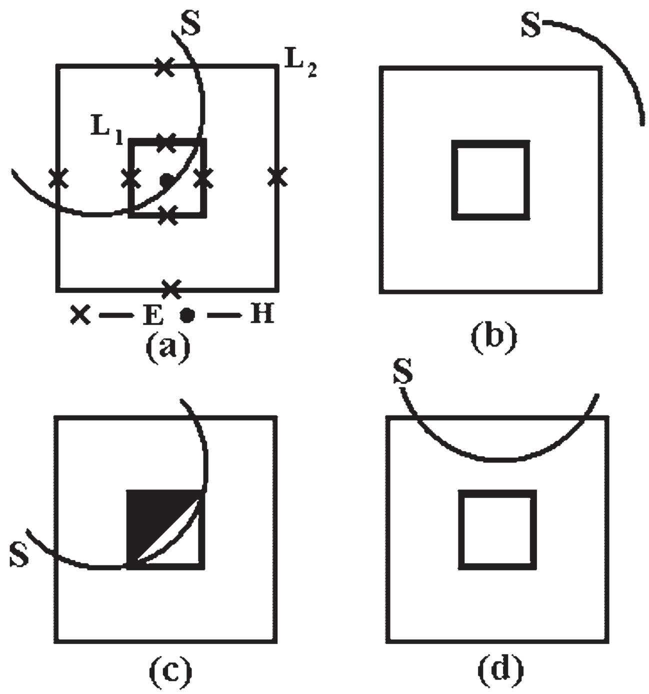

Figure 1 (a) The locations of the H-component and the E-components. (b). Undistorted cell. (c). Completely distorted cell. The black area denotes the diagonal split-cell. (d). Partially distorted cell

$$F_\delta(h) = W_1F_\delta(h) + W_2 \times \left[\frac{1}{2}(F_\delta(h+1) + F_\delta(h-1))\right] \quad (9)$$

where W_1 and W_2 are weighting coefficients satisfying $W_1 + W_2 = 1$. Generally, for $W_1 \in [0.87, 0.97]$, the stable and accurate numerical results can be obtained. Moreover, if the incident plane wave is a unit Gaussian pulse, the largest magnitude of the field values at the partially distorted cells is below the order of 10^{-3}.

4. NUMERICAL RESULTS

Without loss of generality, it can be assumed that the incident plane wave with frequency of 300 MHz propagates along the z direction, and the electric field is polarized along the x direction, and the cubic lattice is adopted.

1. The scattering of conducting cylinder with the radius of $1m$ and the height of $1m$ is considered. The space increment and the CFL number are set to $\Delta_\delta = 0.1m$ and $\mathrm{CFL}_\delta = 0.5$, respectively. The H-plane bistatic RCS plotted in Figure 2 is computed by the SFDTD scheme using the diagonal split-cell model. The result calculated by the diagonal SFDTD scheme is in a good agreement with the reference solution calculated by the moment methods. The absolute RCS error curves are illustrated in Figure 3. It can be seen that the diagonal SFDTD scheme can obtain more accurate results than the staircased SFDTD scheme. Similarly, the relative two-norm error for the diagonal SFDTD

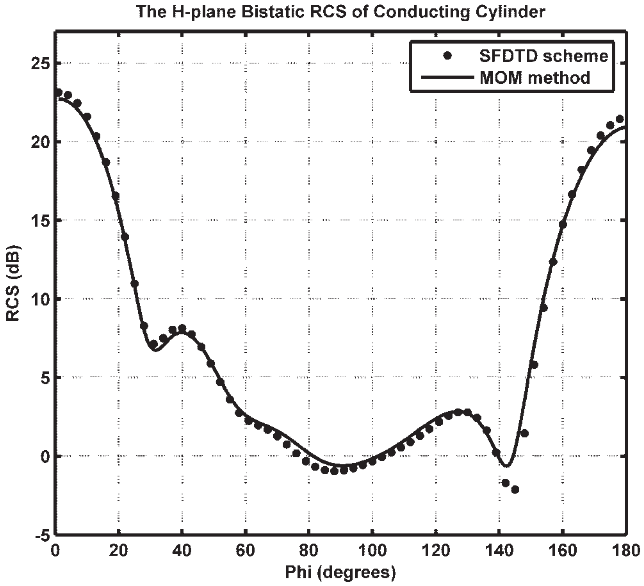

Figure 2 The bistatic RCS of conducting cylinder

scheme is 0.0556 compared with 0.0816 for the traditional diagonal FDTD method.

2. The monostatic RCS of conducting sphere with the radius of 1*m* is calculated. The space increment is unchanged and the CFL number is retaken to $\mathrm{CFL}_\delta = 0.70$. The Figure 4 shows the location of spatial cells for the H_z component. From the Figure 5, because of the utilization of low-order spatial difference near the curved boundaries and the symplectic structure in the time direction, the SFDTD solution at the frequency higher than 300 MHz still keeps accurate and stable after 5000 time steps.
3. The proposed scheme is employed to analyze the far response of conducting prism displayed in Figure 6. The side length of the prism are, respectively, 1*m*, 1*m*, and $\sqrt{2m}$, and the height is chosen to be 1*m*. Under the same relative error condition, the diagonal SFDTD scheme occupies $71 \times 71 \times 71$ cells with $\Delta_\delta = 1.0/8.0$ and $\mathrm{CFL}_\delta = 0.65$, by contrast, the traditional staircased FDTD approach occupies $111 \times 111 \times 111$ cells with $\Delta_\delta = 1.0/15.1$ and $\mathrm{CFL}_\delta = 0.50$. About 32.4% memory and 39.5% CPU time are saved by the proposed scheme.

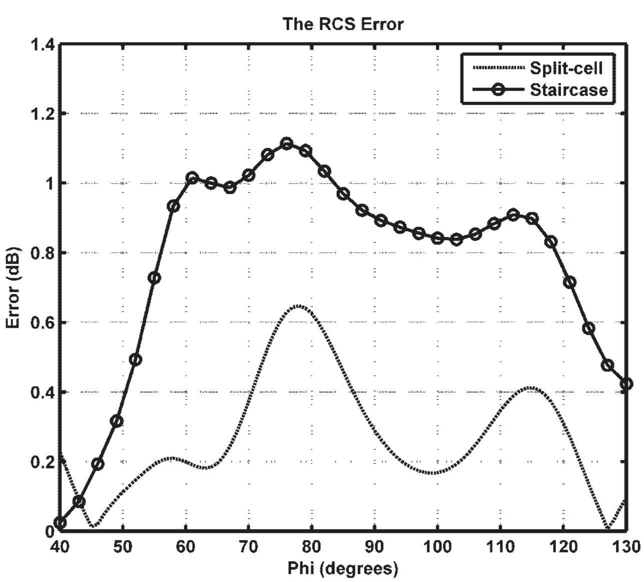

Figure 3 The absolute RCS Error

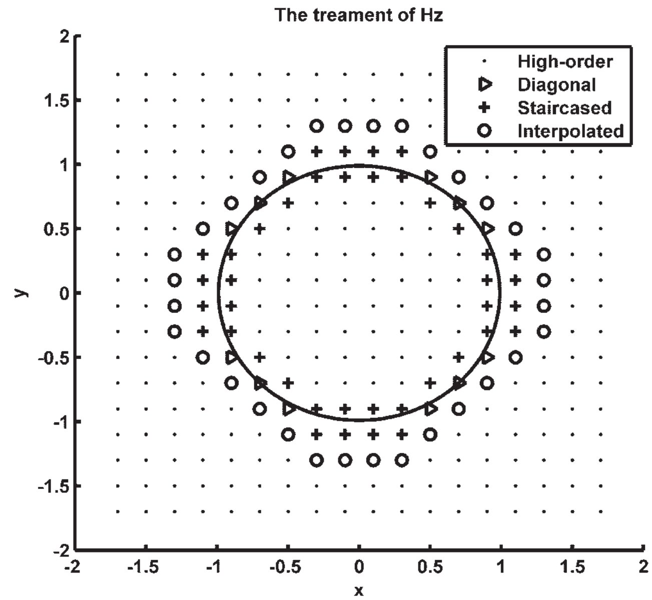

Figure 4 The location of spatial cells for the H_z component. The points denote the undistorted cells, the circles denote the partially distorted cells, and the pluses and triangles denote the completely distorted cells using the staircased and the iagonal approximation

5. CONCLUSION

The high-order SFDTD scheme using the diagonal split-cell model can accurately and efficiently solve the scattering of three-dimensional perfectly conducting objects with curved metal boundaries. The high numerical stability of the scheme can obviate the instability problem due to the traditional diagonal approximation. Furthermore, the improved SFDTD scheme is easy to implement and places little additional computations on the original scheme. The

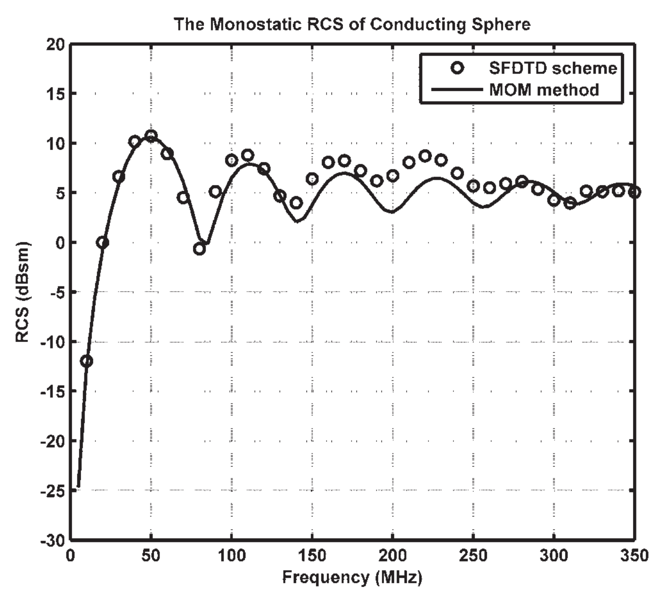

Figure 5 The monostatic RCS of conducting sphere

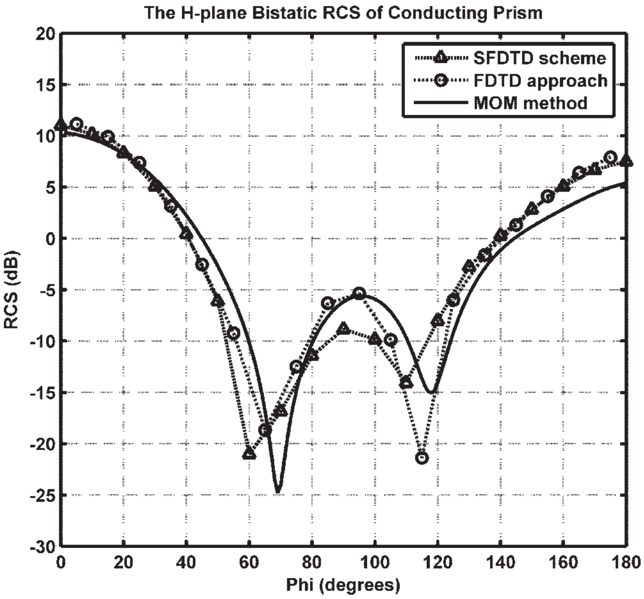

Figure 6 The bistatic RCS of conducting prism

future work will focus on the development of the proposed scheme in conjugation with the subgridding method.

ACKNOWLEDGMENT

This work was supported in part by "The national natural science foundation of China (No. 60371041)."

REFERENCES

1. A. Taflove, Computational electrodynamics: The finite-difference time-domain method, Artech House, Norwood, MA, 1995.
2. J. Fang, Time domain finite difference computation for maxwell's equations, PhD dissertation, Department of Electrical Engineering, University of California, Berkeley, CA, 1989.
3. A. Taflove et al., Advances in computational electrodynamics: The finite-difference time-domain method, Artech House, Norwood, MA, 1998.
4. J.M. Sanz-Serna and M.P. Calvo, Numerical hamiltonian problems, Chapman & Hall, London, UK, 1994.
5. T. Hirono, W. W. Lui, and S. Seki, Successful applications of PML-ABC to the symplectic FDTD scheme with 4th-order accuracy in time and space, IEEE MTT-S Intl Microw Symp Dig 3 (1999), 1293–1296.
6. T. Hirono, W. Lui, S. Seki, and Y. Yoshikuni, A three-dimensional fourth-order finite-difference time-domain scheme using a symplectic integrator propagator, IEEE Trans Microw Theory Tech 49 (2001), 1640–1648.
7. P.W. Zhai, G.W. Kattawar, P. Yang, and C.H. Li, Application of the symplectic finite-difference time-domain method to light scattering by small particles, Appl Opt 44 (2005), 1650–1656.
8. W. Sha, Z.X. Huang, X.L. Wu, and M.S. Chen, Total field and scattered field technique for fourth-order symplectic finite difference time domain method, Chin Phys Lett 23 (2006), 103–105.
9. H. Yoshida, Construction of higher order symplectic integrators, Phys D: Nonlinear Phenomena 46 (1990), 262.
10. P. Mezzanotte, L. Roselli, and R. Sorrentino, A simple way to model curved metal boundaries in FDTD algorithm avoiding staircase approximation, IEEE Microw Guid Wave Lett 5 (1995), 267–269.

A HAIRPIN LINE WIDEBAND BANDPASS FILTER DESIGN WITH EMBEDDED OPEN STUBS

Cheng-Yuan Hung,[1] Min-Hang Weng,[2] Yan-Kuin Su,[1] and Ru-Yuan Yang[1]

[1] Advanced Optoelectronic Technology Center, Institute of Microelectronics, Department of Electrical Engineering, National Cheng Kung University, Taiwan

[2] National Nano Device Laboratories, Taiwan

Received 10 September 2006

ABSTRACT: *In this paper, a compact three-poles hairpin line wide-band bandpass filter with several embedded open stubs to improve the stopband is designed and implemented on print circuit board substrate. This filter at center frequency f_0 of 4.25 GHz has presented almost very good measured characteristics, including the bandwidth of 3.1–5.4 GHz (3-dB fractional bandwidth of 54%), low insertion loss of -0.7 ± 0.4 dB, sharp rejection due to two transmission zeros in the passband edge created by interstage coupling, and wide stopband rejection greater than 15 dB from 5.6 to 11 GHz. Experimental results of the fabricated filter show a good agreement with the predict results.* © 2007 Wiley Periodicals, Inc. Microwave Opt Technol Lett 49: 934–936, 2007; Published online in Wiley InterScience (www.interscience.wiley.com). DOI 10.1002/mop.22302

Key words: *hairpin line; stopband; bandwidth; passband*

1. INTRODUCTION

New ultrawideband radar and high data-rate communication systems require very specialized RF circuits capable of operating over wide frequency ranges [1, 2]. The design of wide-band microwave filters has been a huge challenge over the last few years. Thus, several wideband filter realizations exhibiting an extremely large passband-width have been proposed using different technologies, such as microstrip or uniplanar strip [3, 4]. However, these filters in fact have many problematic issues, such as unexpected slow passband attenuation rate, spurious response, and so on. These filters may use additional bandstop filter or defect ground structure (DGS) to improve out-of-band performance, but also cause the disadvantages, such as additional device area and package problems [5].

In this letter, we report a hairpin line wideband bandpass filter (HL-WBF) with embedded open stubs (OSs), which achieves the advantages of compact size, wide passband, high passband selectivity, and wide out of band (stopband), simultaneously. After optimization the filter design, the designed filter is executed to experimentally verify the simulated results of our design.

2. ANALYSIS OF HL-WBF FILTER

Figure 1 depicts the schematic of the proposed three-poles HL-WBF with embedded OSs. In this paper, a RT/Duroid 5880 substrate with a relative dielectric constant of 2.2, a loss tangent of 0.001, and a thickness of 0.787 mm, is used for the simulation and practical fabrication. The HL-WBF mainly consists of three identical half-guided-wavelength ($\lambda_g/2$) resonators with high-impedance line around 138 Ω and two enhancing coupling input/output ports at the two sides of HL-WBF. The HL-WBF has compact structure by folding the resonators of parallel-coupled, half-wavelength resonator into a "U" shape [6]. Each arm of the folding resonator is coupled each other to achieve strong coupling. The OS is close to a quasi-quarter-wavelength ($\lambda_g/4$) resonator and embedded in central position of folding resonator. Therefore, the fundamental attenuation and several spurious modes of OS can be

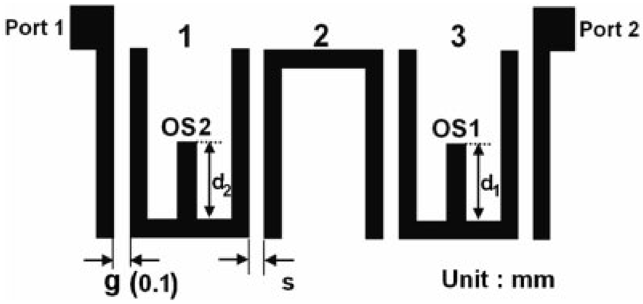

Figure 1 Practical layout of the designed HL-WBF filter with embedded open stubs

created as attenuation poles [7]. In another words, by changing the physical length of the OS, one can control the attenuation poles in the passband edge or stopband of the HL-WBF. Therefore, two modulated parameters, spacing (s) and lengths of the OSs (d_1 and d_2), are used to modulate and achieve the coupling coefficient and stopband in this study, respectively.

A complete full-wave electromagnetic simulator [8] is used for accurate coupling coefficient as functions of the resonator spacing (s). Figure 2 shows the simulated coupling coefficient of two folding resonators. The coupling between folding resonators can be specified by the two dominant resonant modes, which are split off from the resonance condition. The simulated coupling coefficient $K_{i,\ i\ +\ 1}$ between the resonator i and $i + 1$ ($i = 1$ and 2) as functions of spacing (s) is calculated as [6]

$$K_{i,i+1} = \frac{f_{\mathrm{H}}^2 - f_{\mathrm{L}}^2}{f_{\mathrm{H}}^2 + f_{\mathrm{L}}^2} \tag{1}$$

where the f_{H} is the higher frequency of the two resonant modes, and f_{L} is the lower one. It is note that the $K_{i,\ i\ +\ 1}$ is applied by separating off two resonators at a time and that K_{12} and K_{23} are also subject to an offset s. As reducing the s value, the coupling coefficient would be increased, namely, the coupling energy can be enhanced.

A three pole HL-WBF is designed to have a fractional bandwidth of 50% at a central frequency $f_0 = 4$ GHz. A three-pole ($n = 3$) Chebyshev lowpass prototype with a passband ripple of 3 dB is chosen. The lowpass prototype parameters are $g_0 = g_4 = 1$, $g_1 = g_3 = 3.487$, $g_2 = 0.7117$. Having obtained the lowpass parameters,

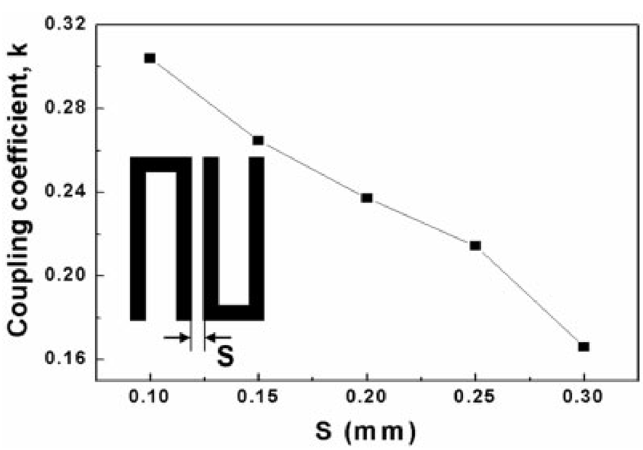

Figure 2 The calculated coupling coefficient of the HL-WBF with different spacing between the folding resonators

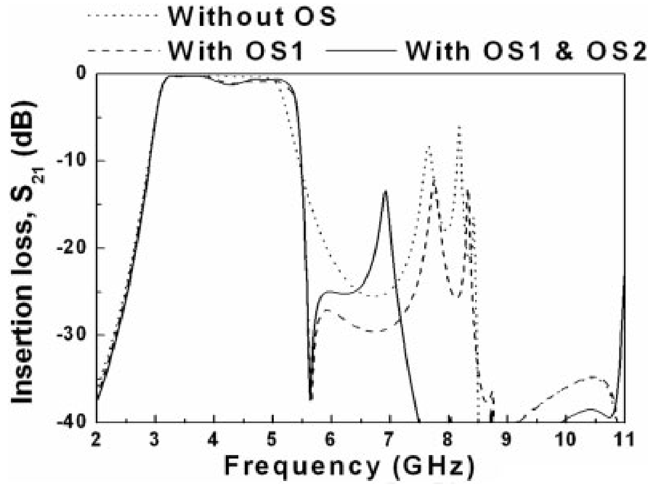

Figure 3 The simulated frequency response of HL-WBF filter without and with embedded open stubs

theoretical coupling coefficient $M_{i,\ i\ +\ 1}$ is obtained as $M_{1,2} = M_{2,3} = 0.3$, calculated by [6]

$$M_{i,i+1} = \frac{\mathrm{FBW}}{\sqrt{g_i g_{i+1}}} \tag{2}$$

Therefore, the spacings between the resonator i and $i + 1$ are also selected as $s_{1,2} = s_{2,3} = 0.1$ mm from Figure 2. To achieve the central frequency $f_0 = 4$ GHz, the length of the half-guided-wavelength ($\lambda_g/2$) resonator is 28.8 mm. The two enhancing coupling input/output ports are designed for 50 Ω and the gap of the two enhancing coupling input/output ports is designed for more enhancing the coupling level of the passband skirt by using a complete full-wave electromagnetic simulation. It is noted that such small gap ($g = 0.1$ mm) between the input/output ports and the resonators is still available by using the conventional carving machine, without using expensive lithography process [3]. Figure 3 shows simulated frequency response of HL-WBF filter without and with OSs. As expected, the slow attenuation rates of passband edge and the spurious response are appeared since the length of resonators in HL-WBF without OS is around the half guided wavelength. Therefore, creation of attenuation poles near the passband edge and harmonics are needed.

In this study, OSs added to the HL-WBF filter are used to produce attenuation poles in the high passband edge and harmonic frequency response; therefore, the proposed HL-WBF filter would have wide stopband and very high passband selectivity performances. Since the OS is close to a quasi-quarter-wavelength ($\lambda_g/4$) resonator, the attenuation pole at 5.6 GHz in the higher passband edge is obtained when the length of one OS (d_1) is 9.9 mm. Thus, the HL-WBF has very high passband selectivity. But, the stopband is not large enough because of insufficient attenuation ability. As the d_1 of OS1 is 9.9 mm and d_2 of OS2 is 5.4 mm, a broad stopband of 5.5–11 GHz is obtained.

3. EXPERIMENTAL RESULTS AND DISCUSSION

Using the above structural parameters, the designed filter was fabricated, as discussed in Figure 4, and then measured by an HP8510C Network Analyzer. Figure 4 shows the picture of the fabricated HL-WBF filter. The whole size of the fabricated HL-WBF filter with OSs is 9.3 mm × 13.2 mm, i.e., approximately

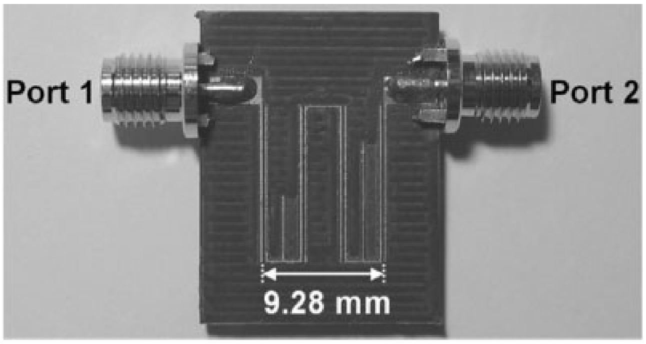

Figure 4 Picture of the fabricated HL-WBF filter

0.17 λ_g by 0.24 λ_g, where λ_g is the guided wavelength at the center frequency.

Figure 5 shows the simulated and measured results of the fabricated filter. The measured results show a center frequency f_0 of 4.25 GHz, very low insertion loss of -0.7 ± 0.4 dB, wide bandwidth of 3.1–5.4 GHz (3-dB fractional bandwidth = 54%) and wide stopband rejection greater than 15 dB from 5.6 to 11 GHz. Moreover, the attenuation poles is clearly observed in the higher side of passband edge at 5.7 GHz with −27 dB attenuation, indicating a selectivity of 100 dB/GHz attenuation slopes in higher passband edge. The measured results verify the possibility of the proposed designed concept, indicating the proposed filter has a good potential for broadband communications, and can be realized on the print circuit board substrate without using expensive lithography process.

4. CONCLUSIONS

In this paper, a three-poles HL-WBF with embedded OSs having high selectivity and wide stopband is reported. By using the OSs, it is able to place attenuation poles near the passband edge so that high passband selectivity with fewer resonators could be obtained. This designed filter was fabricated and measured, showing good characteristics including the bandwidth of 3.1–5.4 GHz (3-dB fractional bandwidth of 54%), low insertion loss of -0.7 ± 0.4, sharp rejection, and wide stopband rejection greater than 15 dB from 5.6–11 GHz.

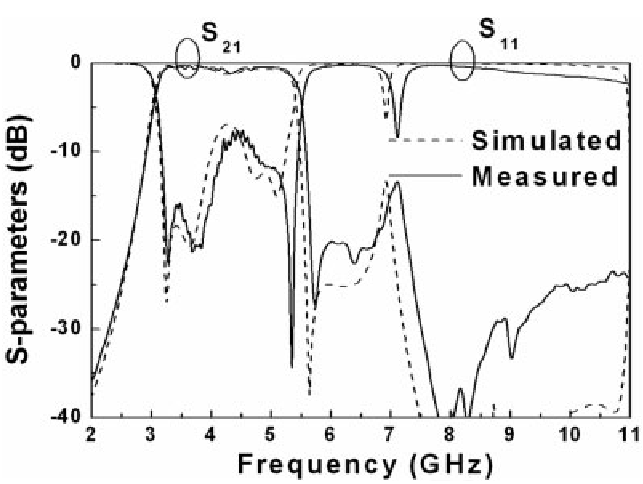

Figure 5 Simulated and measured frequency response of the designed HL-WBF filter. The physical size parameters are as follows: d_1 of OS1 = 9.9 mm and d_2 of OS2 = 5.4 mm. Others parameters are shown in Figure 1

REFERENCES

1. G.G. Roberto and I.A. José, Design of sharp-rejection and low-loss wide-band planar filters using signal-interference techniques, IEEE Trans Microw Theory Tech 15 (2005), 530–532.
2. W. Menzel, L. Zhu, K. Wu, and F. Bögelsack, On the design of novel compact broad-band planar filters, IEEE Trans Microw Theory Tech 51 (2003), 364–370.
3. C.C. Chen, J.T. Kuo, M. Jiang, and A. Chin, Study of parallel coupled-line microstrip filter in broadband, Microw Opt Tech Lett 48 (2006), 373–375.
4. G.L. Matthaei, Interdigital band-pass filters, IEEE Trans Microw Theory Tech 10 (1962), 479–491.
5. H.W. Wu, M. H. Weng, Y.K. Su, R.Y. Yang, and C.Y. Hung, Spurious suppression of a parallel coupled microstrip bandpass filter with simple ring EBG cells on the middle layer, IEICE Trans Electron Lett E89-C (2006), 568–570.
6. J.S. Hong and M.J. Lancaster, Development of new microstrip pseudo-interdigital bandpass filters, IEEE Microw Guid Wave Lett 5 (1995), 261–263.
7. J.R. Lee, J.H. Cho, and S.W. Yun, New compact bandpass filter using microstrip λ/4 resonators with open stub inverter, IEEE Microw Guid Wave Lett 10 (2000), 526–527.
8. Zeland Software, Inc., IE3D Simulator, 1997.

HIGH-PERFORMANCE SINGLE-TURN INTERLACED-STACKED TRANSFORMERS FOR KA-BAND CMOS RFIC APPLICATIONS

Yo-Sheng Lin,[1] Chi-Chen Chen,[1] Hsiao-Bin Liang,[1] Po-Feng Yeh,[1] Tao Wang,[2] and Shey-Shi Lu[2]
[1] Department of Electrical Engineering, National Chi-Nan University, Puli, Taiwan, Republic Of China
[2] Department of Electrical Engineering, National Taiwan University, Taipei, Taiwan, Republic Of China

Received 10 September 2006

ABSTRACT: *In this article, we demonstrate that high-coupling and ultra-low-loss transformers for Ka-Band (26–40 GHz) CMOS RFIC applications can be achieved by using single-turn interlaced-stacked (STIS) structure implemented in a standard 0.18-μm CMOS technology. State-of-the-art G_{Amax} of 0.777, 0.852, and 0.799 (i.e., NF_{min} of 1.097, 0.695, and 0.977 dB) were achieved at 30, 36, and 40 GHz, respectively, for a 2-layer STIS transformer with an inner dimension of 100 × 100 μm² and a metal width of 10 μm, mainly due to the high magnetic-coupling factor and the high resistive-coupling factor. Furthermore, the reasons why the STIS transformer exhibits better performances than the traditional bifilar and the traditional stacked transformer are explained. These results show that the STIS transformers are very promising for high-performance Ka-Band CMOS RFIC applications.* © 2007 Wiley Periodicals, Inc. Microwave Opt Technol Lett 49: 936–942, 2007; Published online in Wiley InterScience (www.interscience.wiley.com). DOI 10.1002/mop.22301

Key words: *magnetic-coupling; resistive-coupling; single-turn; interlaced; stacked; transformer*

1. INTRODUCTION

Recently, RF CMOS and BiCMOS processes have become more and more popular for RF-ICs operated in the 24–100 GHz frequency band [1–4]. In the design of ultra-low-voltage high-performance VCOs [5, 6] and LNAs [7], the power gain G_A (or noise figure NF) performance of the transformers used is crucial for the